Draft version October 18, 2019
Typeset using LaTeX **twocolumn** style in AASTeX61

COMPOSITIONS OF PLANETARY DEBRIS AROUND DUSTY WHITE DWARFS

Siyi Xu (许偲艺),[1] Patrick Dufour,[2,3] Beth Klein,[4] Carl Melis,[5] Nathaniel N. Monson,[6] B. Zuckerman,[4] Edward D. Young,[6] and Michael A. Jura[4,*]

[1] *Gemini Observatory, 670 N. A'ohoku Place, Hilo, HI 96720*
[2] *Département de Physique, Université de Montréal, C.P. 6128, Succ. Centre-Ville, Montréal, Québec H3C 3J7, Canada*
[3] *Institut de Recherche sur les Exoplanètes (iREx), Université de Montréal, Montréal, QC H3C 3J7, Canada*
[4] *Department of Physics and Astronomy, University of California, Los Angeles, CA 90095-1562, USA*
[5] *Center for Astrophysics and Space Sciences, UCSD, CA 92093-0424, USA*
[6] *Department of Earth, Planetary, and Space Sciences, University of California, Los Angeles, CA 90095, USA*

ABSTRACT

The photospheres of some white dwarfs are "polluted" by accretion of material from their surrounding planetary debris. White dwarfs with dust disks are often heavily polluted and high-resolution spectroscopic observations of these systems can be used to infer the chemical compositions of extrasolar planetary material. Here, we report spectroscopic observation and analysis of 19 white dwarfs with dust disks or candidate disks. The overall abundance pattern very much resembles that of bulk Earth and we are starting to build a large enough sample to probe a wide range of planetary compositions. We found evidence for accretion of Fe-rich material onto two white dwarfs as well as O-rich but H-poor planetary debris onto one white dwarf. In addition, there is a spread in Mg/Ca and Si/Ca ratios and it cannot be explained by differential settling or igneous differentiation. The ratios appear to follow an evaporation sequence. In this scenario, we can constrain the mass and number of evaporating bodies surrounding polluted white dwarfs.

Keywords: stars: abundances – white dwarfs: circumstellar matter – minor planets, asteroids

Corresponding author: Siyi Xu
sxu@gemini.edu

* Deceased

1. INTRODUCTION

Thanks to radial velocity, transit, and microlensing surveys, we now know that planetary systems are prevalent around main-sequence stars (e.g. Petigura et al. 2013). Naturally, this has lead to great interest in performing detailed characterization of extrasolar planetary systems. Using mass-radius relationships, we can differentiate between rocky planets, ocean planets, and planets with an extended atmosphere (Zeng et al. 2016). However, planet models become increasingly degenerate with little difference in planet mass-radius relationships when including minor and trace elements (e.g. Dorn et al. 2015). Luckily, we can get around this limitation by observing "polluted" white dwarfs (WDs), which are accreting from extrasolar planetary debris.

Recent studies show that planetary systems can be present around WDs (Mustill & Villaver 2012; Nordhaus & Spiegel 2013). From different dynamical interactions, i.e. planet-planet scattering, mean motion resonance, and Kozai-Lidov effect, minor planets can be perturbed to enter into the tidal radius of the WD and subsequently be disrupted (e.g. Debes & Sigurdsson 2002; Frewen & Hansen 2014; Stephan et al. 2017). Eventually, all these planetary debris will settle into a disk of dust and gas. Dust disks around WDs can be detected via an infrared excess because most of the WD light is in the UV/optical (e.g. Jura et al. 2007). Circumstellar gas material can manifest itself as either emission or absorption, depending on the inclination of the disk (e.g. Gänsicke et al. 2006, 2012; Debes et al. 2012).

Thereafter, the circumstellar dust and gas will be accreted onto the WD, polluting its atmosphere. Because the outermost layer of WDs typically consist of pure hydrogen (DA) or helium (DB), even a small amount of heavy elements can create a detectable spectroscopic signature and the constituent elements can be measured individually to a high precision (e.g. Zuckerman et al. 2007). Spectroscopic studies of these polluted WDs can be used to infer the bulk compositions of extrasolar planetary material, which is not possible with any other technique (Jura & Young 2014).

A direct support for this asteroid disruption model is the discovery of an actively disintegrating asteroid transiting WD 1145+017 near the tidal radius (Vanderburg et al. 2015). Recently, it has been suggested that there is a planetesimal in a 2-hr orbit around WD 1226+110 (Manser et al. 2019). Not surprisingly, both WD 1145+017 and WD 1226+110 have a circumstellar dust and gas disk and they are heavily polluted (Gänsicke et al. 2012; Brinkworth et al. 2012; Xu et al. 2016).

To zeroth order, the compositions of extrasolar planets accreted onto WDs resemble that of bulk Earth – O, Fe, Si, and Mg are often the dominant elements (Xu et al. 2014). Planets with exotic compositions that have no solar system analogs, such as refractory-rich planets or carbon-rich planets, have yet to be found (Jura & Xu 2013; Wilson et al. 2016). In a volume-limited sample of DBs, the fraction of water is less than 1% of the total accreted mass (Jura & Xu 2012) even though there are some exceptions where the WDs have accreted a significant amount of water (e.g. Farihi et al. 2013; Raddi et al. 2015; Gentile Fusillo et al. 2017). At least one WD has accreted a Kuiper-Belt-Object analog with 30% water and 10% carbon by mass (Xu et al. 2017). Differentiation and collisions also appear to be common in extrasolar planetary systems (Jura et al. 2013; Harrison et al. 2018).

Identifying and analyzing heavily polluted WDs is crucial to our understanding of the chemical compositions of extrasolar planets. Even though hundreds of polluted WDs have been identified, most of them only show calcium absorption in the optical (Zuckerman et al. 2003; Koester et al. 2005; Dufour et al. 2007; Hollands et al. 2018). The most heavily polluted WDs often display excess infrared radiation from an orbiting dust disk (von Hippel et al. 2007). Dusty WDs are promising targets to detect multiple elements – the focus of this study.

In this paper, we report results from high resolution spectroscopic observations of 13 WDs with circumstellar dust disks and 6 disk candidates. Due to different false positives, WDs with infrared excesses are considered as disk candidates in this work unless a *Spitzer* observation exists to confirm the disk nature of the infrared excess. In this sample, 16 WDs are DAs, 2 are DBs, and 1 is a DZ[1]. Most of the observations were performed at the *Keck Telescope*; one southern object was observed with the *Very Large Telescope* (*VLT*) and another system with the *Hubble Space Telescope* (*HST*). The paper is organized as follows. Observations and data reduction are described in Section 2. Abundance analysis is presented in Section 3 and the results are discussed in Section 4. Conclusions are presented in Section 5.

2. OBSERVATIONS

2.1. *Keck/HIRES*

The majority of WDs in our sample were observed with the High Resolution Echelle Spectrometer (HIRES) on the *Keck I Telescope* (Vogt et al. 1994), which

[1] Based on the spectroscopic classification, WD 1232+563 is a DZBA because the strongest optical absorption feature is Ca II-K.

has a blue collimator (HIRESb) and a red collimator (HIRESr). For both collimators, the C5 decker was used, which gives a spectral resolution of $\sim$ 40,000. The typical wavelength coverage is 3200–5750 Å and 4700–9000 Å for HIRESb and HIRESr, respectively. Following our previous HIRES observations, data reduction was performed by using the MAKEE package and then continuum normalization with IRAF (Klein et al. 2010; Xu et al. 2016). The observing log and some representative spectra are shown in the Appendix.

2.2. *Keck/ESI*

Some of the WDs were observed with the Echellette Spectrograph and Imager (ESI) on the *Keck II Telescope* (Sheinis et al. 2002). A slit width of 0.″3 was used with a spectral resolution of 14,000. The wavelength coverage is 3900–10,000 Å. Data reduction was performed with MAKEE and IRAF, similar to the HIRES reduction process.

Compared to HIRES, ESI has a lower spectral resolution but a wider wavelength coverage. ESI is more efficient at studying faint heavily polluted WDs, e.g. WD 1232+563. However, ESI has no transmission shortward of 3900 Å and the throughput is very poor around Ca II K 3933 – the most important absorption line in the optical. HIRESb is crucial for detecting lines between 3200 and 4000 Å.

2.3. *VLT/UVES*

WD 0107-192 was observed with the Ultraviolet and Visual Echelle Spectrograph (UVES) on the *VLT* under program 096.C-0132 (Dekker et al. 2000). The dichroic beam splitter was used, which allows for simultaneous observations with both the blue and the red arms. For the blue arm, the CD#2 grating was used with a wavelength coverage of 3300–4500 Å while for the red arm, the CD#4 grating was used with a wavelength coverage of 5700–9400 Å. A slit width of 1.″0 was chosen, which gives a spectral resolution of 22,000. Data reduction was performed using the UVES pipeline.

2.4. *HST/COS*

PG 0010+280 is the hottest dusty WDs known and optical observations with HIRES only returned upper limits (Xu et al. 2015). Here, we report UV spectroscopic observations with the Comic Origins Spectrograph (COS) onboard the *HST* (Program ID #14117). The G130M grating was used with a central wavelength of 1291 Å, which gives a wavelength coverage of 1150–1430 Å with a 20 Å gap in the middle. To minimize the fixed-pattern noise, all four FP-POS steps are used (COS Instrument Handbook). Data reduction was performed with the CALCOS pipeline.

Table 1. WD Parameters

Name	Atm.	T (K)	Log g	Ref [a]
G 166-58	H	7390 ± 200	7.99 ± 0.10	(1,2)
WD 2221-165	H	10130 ± 200	8.15 ± 0.10	(3,4)
WD 0307+077	H	10230 ± 200	7.96 ± 0.10	(3,4)
PG 1541+651	H	11880 ± 200	8.20 ± 0.10	(1,5)
WD 1145+288[b]	H	12140 ± 210	8.14 ± 0.10	(3,6)
WD 1150-153	H	12640 ± 200	8.22 ± 0.10	(1,7)
GD 56	H	15270 ± 300	8.09 ± 0.10	(1,8)
WD 0107-192[b]	H	15440 ± 300	7.95 ± 0.10	(1,9)
HE 0106-3253	H	17350 ± 200	8.12 ± 0.10	(3,4)
PG 1015+161	H	20420 ± 350	8.11 ± 0.10	(1,8)
PG 1457-086[b,c]	H	22240 ± 400	7.99 ± 0.10	(1,9,10)
WD 1226+110	H	23500 ± 200	8.16 ± 0.10	(11,12)
PG 1018+411	H	24440 ± 400	8.11 ± 0.10	(1,13)
PG 0843+517	H	24670 ± 400	7.93 ± 0.10	(1,14)
WD 1341+036[b]	H	26420 ± 200	7.85 ± 0.10	(11,15)
PG 0010+280[b]	H	27220 ± 400	7.87 ± 0.10	(1,16)
WD 1232+563[b]	He	11787 ± 423[b]	8.30 ± 0.06	(17)
WD 1551+175	He	14756 ± 1286	8.02 ± 0.12[b]	(3,18)
WD 2207+121	He	14752 ± 1192	7.97 ± 0.12[b]	(17,14)

NOTE—(1) Gianninas et al. (2011); (2) Farihi et al. (2008); (3) *This paper*; (4) Farihi et al. (2010); (5) Kilic et al. (2012); (6) Barber et al. (2014); (7) Kilic & Redfield (2007); (8) Jura et al. (2007); (9) Dennihy et al. (2017); (10) Farihi et al. (2009); (11) Tremblay et al. (2011); (12) Brinkworth et al. (2009); (13) Barber et al. (2016); (14) Xu & Jura (2012); (15) Li et al. (2017); (16) Xu et al. (2015); (17) Coutu et al. (2019); (18) Bergfors et al. (2014)

[a] The first reference is for the WD parameters and the second is for the infrared excess.

[b] Disk candidates.

[c] This object has *Spitzer* photometry. However, there is a red background object within 1 arcsec and the photometry is likely to be contaminated (Dennihy et al. 2017).

3. DATA ANALYSIS

3.1. *Stellar Parameters*

The stellar parameters for most DAs are taken from previous studies using a spectroscopic method (Gianninas et al. 2011; Tremblay et al. 2011) – it compares the profiles of normalized Balmer lines with WD models until a good match is found. The uncertainties quoted

in those works are only statistical uncertainties from the fit, which could underestimate the true uncertainties. Here, we adopt a more conservative uncertainty of at least 200 K in temperature and 0.1 dex in log g. For WDs not in these two studies, we performed our own spectroscopic fit with the *SDSS* spectra or other archival spectra using models from the Montreal white dwarf group following the same procedures outlined in these two papers. Our adopted parameters, after applying 3D corrections (Tremblay et al. 2011), are listed in Table 1.

The analysis of DBs and DZs are a more interactive process. Following the methods developed in Dufour et al. (2007) and Coutu et al. (2019), we started with finding the best WD parameters that would fit the *SDSS* photometry and parallax from *Gaia* while also including hydrogen and heavy elements. Then we used this set of parameters as the starting point to do an interactive fitting of the *SDSS* spectrum by varying temperature, log g, H and Ca abundances[2]. This whole process is repeated several times until the parameters have converged to a stable solution (see Coutu et al. 2019 for details). The derived WD parameters are listed in Table 1.

3.2. *Abundance Determination*

To determine the abundances of heavy elements, we calculated synthetic spectra using the WD atmospheric structure computed in section 3.1. In each iteration, a grid of spectra with different abundances for the element of interest were calculated while keeping the abundances of all the other elements the same. Each model spectrum was compared with the data and the final abundance is adopted from the model returning the minimum χ^2. This process is repeated for each heavy element for all the DAZs. Some representative fits are shown in the Appendix.

If only one absorption line is detected for a heavy element, the abundance uncertainty mostly comes from the quality of the spectrum. Most elements have more than one detected line and the uncertainty is dominated by the different abundances derived when using different spectral lines. In addition, to estimate the impact of stellar parameters, we computed abundances of heavy elements with a five-grid WD model with parameters of (T, log g), (T+ΔT, log g), (T-ΔT, log g), (T, log g + Δ log g), and (T, log g - Δ log g). The final abundances and uncertainties listed in Table 2 are the average values from these five models. The accretion rates are listed in Table 3. We consider the abundance uncertainties to be fairly conservative, as they include both the measurement error and systematic error from WD parameters.

For DBZs and DZs, the presence of heavy elements could also have an impact on the thermal structure of a WD model. Sometimes, it is necessary to repeat the processes outlined in section 3.1 to obtain a self-consistent solution. It has been demonstrated that this method works well even for heavily blended regions, e.g. WD J0738+1835 (Dufour et al. 2012). Some representative fits are shown in the Appendix and the abundances and accretion rates are reported in Table 4.

PG 0010+280 is the only WD with UV spectra in this sample. Our model can reasonably reproduce the strength of Si III and Si IV lines, as shown in the Appendix. However, we found a big discrepancy of carbon abundances derived from C II and C III, likely because the atmosphere is stratified due to gravitational settling and radiative levitation (Koester et al. 2014). The equivalent width of Si II 1265 Å and C II 1335 Å lines are 34 mÅ and 81 mÅ, respectively; this is within the range that can be supported by radiative levitation and no ongoing external accretion is required to explain the heavy elements in the atmosphere (Koester et al. 2014).

3.3. *Optical and UV Discrepancy*

The abundances of three DAZs (PG 1015+161, WD 1226+110, and PG 0843+517) analyzed here have been reported in a previous study with UV spectroscopy (Gänsicke et al. 2012). We find some discrepancies between optical and UV abundances, as listed in Table 5. In these three DAZs, the optical Si and Fe abundances are always higher than those derived from the UV data. The most extreme case is Si in PG 1015+161, where the optical abundance is a factor of 10 higher than that in the UV. We have identified five other systems from the literature where optical and UV determinations of the same element exist. For two of the DBZs (GD 40 and G 241-6), their optical Si abundances are lower than the UV abundances – opposite of what we found here for the DAZs. The Si abundances in the other two DBZs (GD 61 and Ton 345) agree within the uncertainties between the optical and UV.

The optical and UV data are often analyzed in different studies and the adopted WD parameters are different, which could be the cause of the discrepancy. We made some preliminary tests and found that we can reproduce the reported abundances using the reported WD parameters. This suggests that this problem is likely to be present in all the WD models used for abundance analysis. Fortunately, the abundance ratios

[2] The other heavy elements are included assuming the composition of CI chondrites.

Table 2. Abundances of DAZs

Name	Velocity (km s^{-1})	log n(Mg)/n(H)	log n(Si)/n(H)	log n(Ca)/n(H)	log n(Fe)/n(H)	log n(Z)/n(H)
G 166-58	29.1 ± 1.0	-8.06 ± 0.05	< -8.20	-9.33 ± 0.08	-8.22 ± 0.13	Ni -9.50 ± 0.20
WD 2221-165	45.9 ± 1.0	-7.00 ± 0.20	< -5.00	-7.52 ± 0.15	< -5.90	...
WD 0307+077	98.4 ± 1.1	-6.58 ± 0.07	< -5.50	-7.10 ± 0.14	< -6.30	...
PG 1541+651	102 ± 1.0	< -6.50	< -5.70	-7.36 ± 0.08	< -6.00	...
WD 1145+288	41.7 ± 1.5	-6.00 ± 0.20	< -4.70	-6.88 ± 0.08	-5.43 ± 0.20	...
WD 1150-153	21.8 ± 1.8	-6.14 ± 0.20	< -5.50	-7.03 ± 0.20	< -5.70	...
GD 56	19.5 ± 2.1	-5.55 ± 0.20	-5.69 ± 0.20	-6.86 ± 0.20	-5.44 ± 0.20	...
WD 0107-192	33.6 ± 2.0	< -6.40	< -5.20	-7.77 ± 0.20	< -4.70	...
HE 0106-3253	55.9 ± 1.0	-5.57 ± 0.20	-5.48 ± 0.05	-5.93 ± 0.11	-4.70 ± 0.06	...
PG 1015+161	68.2 ± 1.0	-5.60 ± 0.20	-5.42 ± 0.21	-6.40 ± 0.20	-4.92 ± 0.20	...
PG 1457-086	22.6 ± 1.0	-5.47 ± 0.20	-5.85 ± 0.20	-6.23 ± 0.20	< -5.0	...
WD 1226+110	38.5 ± 2.5	-4.52 ± 0.20	-4.64 ± 0.15	-5.26 ± 0.16	< -4.50	...
PG 1018+411	30.5 ± 2.0	-4.86 ± 0.20	-5.36 ± 0.20	< -5.00	< -4.30	...
PG 0843+517	81.1 ± 3.1	-4.82 ± 0.20	-4.59 ± 0.12	-6.26 ± 0.20	-3.84 ± 0.18	...
WD 1341+036	...	< -6.00	< -5.50	< -4.50	< -4.50	...
PG 0010+280	40.9 ± 5.8	...	-7.51 ± 0.15	...	...	C -6.75/-8.01[a] ± 0.15

[a]The carbon abundance of -6.75 is derived from using C II lines while -8.01 is from C III lines.

Note—Spectral lines used for abundance analysis: Mg I 3832.3 Å, 3838.3 Å, 5172.7 Å, 5183.6 Å, Mg II 4481 doublet, Si II 3856.0 Å, 3862.6 Å, 4128.1 Å, 4130.9 Å, 5041.0 Å, 5056.0 Å, 6347.1 Å, 6371.4 Å, Ca I 4226.7 Å, Ca II 3158.9 Å, 3179.3 Å, 3706.0 Å, 3736.9 Å, 3933.7 Å, 3968.5 Å, 8498.0 Å, 8542.1 Å, 8662.1 Å, Fe I 3734.9 Å, 3859.9 Å, Fe II 3213.3 Å, 3227.7 Å, 4233.2 Å, 4923.9 Å, 5018.4 Å, 5169.0 Å. For G166-58, we also used many Fe I lines between 3400–3900 Å. For PG 0010+280, we used C II 1334.5 Å, 1335.7 Å, many C III lines around 1175 Å, Si II 1260.4 Å, 1264.7 Å, Si III 1294.5 Å, 1296.7 Å, 1298.9 Å, Si IV 1393.8 Å, 1402.8 Å.

vary much less. For one of the most extreme cases, log n(Fe)/n(Si) is 0.5 in PG 0843+517 in the optical while this number goes up to 0.9 in the UV.

We acknowledge that this presents a challenge in using polluted WDs to derive the chemical compositions of extrasolar planetesimals. This problem only starts to appear when an element is detected both in the optical and UV. There are only eight such systems now and the results are inconclusive. More observations and analysis are needed to understand the extent of this discrepancy. Gänsicke et al. (2012) discussed three possibilities for this discrepancy, i.e. uncertain atomic data, abundance stratification, and genuine variation. They concluded that abundance stratification is the most likely cause. Indeed, this problem is likely related to the atmospheric structure calculation, because optical and UV lines originate from different depths of the WD atmosphere. Solving the optical and UV discrepancy is beyond the scope of current study and will be explored in future work.

3.4. *Circumstellar Gas*

WD 1226+110 and WD 1341+036 have been reported to display calcium infrared triplet emission from circumstellar gas material (Gänsicke et al. 2006; Li et al. 2017). Such gas has been detected around 20% of dusty WDs and it is a result of collision and evaporation of planetesimals. The emission lines can be variable on time-scales of a few years (Wilson et al. 2014; Manser et al. 2016; Dennihy et al. 2018).

For WD 1341+036, no calcium infrared triplet emission was detected in the ESI data. A closer inspection of the original *SDSS* discovery spectrum shows that there are strong sky lines at the same wavelengths, as shown in Fig. 1. Likely, the weak emission was due to improper sky subtraction rather than the presence of circumstel-

Table 3. Accretion Rates of DAZs

Name	Mg (g s^{-1})	Si (g s^{-1})	Ca (g s^{-1})	Fe (g s^{-1})
G 166-58	5.6× 10^{6}	<4.6×10^{6}	5.2×10^{5}	1.3×10^{7}
WD 2221-165	2.7× 10^{7}	<3.0×10^{9}	1.3×10^{7}	<1.1×10^{9}
WD 0307+077	4.5× 10^{7}	<6.1×10^{8}	2.2×10^{7}	< 2.7×10^{8}
PG 1541+651	<1.9×10^{7}	<8.1×10^{7}	4.1×10^{6}	< 1.4×10^{8}
WD 1145+288	3.2×10^{7}	<4.0 ×10^{8}	7.1×10^{6}	2.8×10^{8}
WD 1150-153	1.0×10^{7}	<4.3 ×10^{7}	2.7×10^{6}	<1.0×10^{8}
GD 56	1.0×10^{7}	1.3×10^{7}	1.3×10^{6}	1.1×10^{9}
WD 0107-192	<1.2×10^{6}	<3.4×10^{7}	1.3×10^{5}	<3.9×10^{8}
HE 0106-3253	8.9× 10^{6}	2.0×10^{7}	9.9×10^{6}	4.4×10^{8}
PG 1015+161	9.3× 10^{6}	2.1×10^{7}	4.0×10^{6}	2.5×10^{8}
PG 1457-086	1.2× 10^{7}	6.8×10^{6}	5.9×10^{6}	<9.2×10^{7}
WD 1226+110	1.4× 10^{7}	1.4×10^{8}	6.9×10^{7}	<7.2×10^{8}
PG 1018+411	6.3× 10^{7}	2.4×10^{7}	<1.2×10^{8}	<1.1×10^{9}
PG 0843+517	5.7× 10^{7}	1.1×10^{8}	5.7×10^{6}	2.4×10^{9}
WD 1341+036	< 3.7× 10^{6}	<1.2×10^{7}	<3.3×10^{8}	<4.4×10^{8}
PG 0010+280	...	1.1× 10^{5}	..	....

Note—The accretion rates are calculated based on abundances reported in Table 2 and diffusion timescales from the Montreal White Dwarf Database (Dufour et al. 2017).

lar gas. For WD 1226+110, the HIRES data covering the calcium triplet emission feature have been discussed in Melis et al. (2010) and we will not repeat the analysis here. No other WDs analyzed in this sample display calcium triplet emission lines.

4. DISCUSSION

4.1. *Overall Abundance Pattern*

We have detected 8, 9, and 10 heavy elements from the optical spectra of WD 1232+563, WD 1551+171, and WD 2207+121, respectively. Together with 18 other polluted WDs, there now are 21 WDs in total where all the major rock forming elements (i.e. Mg, Si, Ca, Fe, and O) are detected. The 18 systems are G29-38, WD J0738+1835, HS 2253+8023, G241-6, GD 40, GD 61, PG 1015+161, WD 1226+110, WD 1929+012, PG 0843+517, Ton 345, SDSS 1242+5226, WD 1425+540, WD 1145+017, SDSS J1043+0855, WD 1536+520, WD 0446-255 and WD 1350-162 (Klein et al. 2011; Dufour et al. 2012; Gänsicke et al. 2012; Jura et al. 2012; Wilson et al. 2015; Farihi et al. 2013; Xu et al. 2013; Jura et al. 2015; Raddi et al. 2015; Farihi 2016; Melis & Dufour 2017; Xu et al. 2017; Swan et al. 2019).

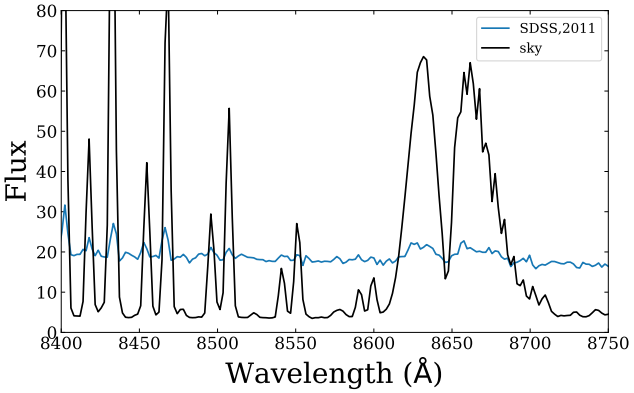

Figure 1. SDSS spectra of WD 1341+036 (ID: 4786-55651-0056). The strongest calcium emission at 8662 Å was marginally detected. However, that wavelength also has strong sky lines and the emission is likely due to improper sky subtraction. The calcium triplet emission line was not detected in our ESI data.

There are 14 DBZs and except for WD 1425+540, all five major elements are measured in the optical. While for DAZs, aside from WD 1929+012 (Vennes et al. 2010), ultraviolet (UV) spectroscopy is needed to mea-

Table 4. Abundances and Accretion Rates of DBZs and DZs

	WD 1232+563			WD 1551+175			WD 2207+121		
	log n(Z)/n(He)	M(Z) (10^{20}g)	$\dot{M}(Z)$ (10^8 g s^{-1})	log n(Z)/n(He)	M(Z) (g) (10^{20}g)	$\dot{M}(Z)$ (10^8 g s^{-1})	log n(Z)/n(He)	M(Z) (g) (10^{20}g)	$\dot{M}(Z)$ (10^8 g s^{-1})
H	-5.90 ± 0.15	5.80	...	-4.45 ± 0.08	219.47	...	-6.32 ± 0.15	3.52	...
O	-5.14 ± 0.15	528.29	33.57	-5.48 ± 0.15	323.60	11.89	-5.32 ± 0.15	557.96	16.43
Mg	-6.09 ± 0.05	89.63	5.47	-6.29 ± 0.05	75.79	2.77	-6.15 ± 0.10	126.24	3.71
Al	< -7.50	< 3.91	< 0.24	-6.99 ± 0.15	16.90	0.64	-7.08 ± 0.15	16.58	0.50
Si	-6.36 ± 0.13	56.53	3.40	-6.33 ± 0.10	79.87	3.00	-6.17 ± 0.11	139.95	4.23
Ca	-7.69 ± 0.05	3.77	0.38	-6.93 ± 0.07	28.50	1.59	-7.40 ± 0.08	11.65	0.52
Ti	-8.96 ± 0.11	0.24	0.03	-8.68 ± 0.11	0.62	0.04	-8.84 ± 0.14	0.51	0.02
Cr	-8.16 ± 0.07	1.64	0.17	-8.25 ± 0.07	1.80	0.11	-8.16 ± 0.19	2.62	0.12
Mn	-8.54 ± 0.05	0.73	0.08	-8.74 ± 0.05	0.61	0.04	-8.50 ± 0.08	1.26	0.06
Fe	-6.45 ± 0.11	90.73	9.18	-6.60 ± 0.10	85.68	4.85	-6.46 ± 0.13	142.72	6.48
Ni	< -7.30	< 13.47	< 1.28	< -7.50	< 11.34	< 0.62	-7.55 ± 0.20	12.11	0.53
$\sum^a$	...	771.55	52.50	...	613.38	24.92	...	1011.61	32.61

[a] The total mass and accretion rate exclude H.

NOTE—The average radial velocity is 19.0 ± 2.0 km s^{-1}, 22.9 ± 1.5 km s^{-1}, and 34.5 ± 2.0 km s^{-1} for WD 1232+563, WD 1551+175 and WD 2207+121, respectively.

sure all the major elements. Dusty DBZs are the best candidates for detecting multiple heavy elements from the ground.

For this sample of dusty WDs and candidates, the accretion is likely to be on-going and the WD's atmosphere is possibly dominated by one large parent body. Assuming a steady state accretion, we can calculate the mass fraction for each element, as shown in Fig. 2. Even though the exact proportions are different, O, Fe, Si and Mg make up at least 87% of the total mass for 19 out of 21 WDs, very similar to the composition of bulk Earth. In two systems, carbon comprises a significant fraction of the total mass – 11% for WD 1425+540 and 15% for Ton 345 from the optical and 2.6% from the UV (see discussion in Section 3.3). WD 1425+540 has accreted a significant amount of O, C, and N as well and it has been proposed that the parent body was a Kuiper-Belt-Object analog (Xu et al. 2017). In contrast, Ton 345 has barely accreted enough O to form O-bearing minerals in both optical and UV studies. It has been suggested that the parent body was similar to anhydrous interplanetary dust particles (IDP; Jura et al. 2015).

Now we comment on some WDs analyzed in this study.

WD 1232+563: accretion from an O-rich & H-poor parent body. Oxygen is 64% of the total material by mass. Indeed, there is more oxygen than is needed to form MgO, SiO_2, Fe_2O_3[3], CaO, and Al_2O_3; 57% of the O is uncombined following procedures outlined in Klein et al. (2010). As a result, H_2O is the next most likely carrier of oxygen. There are three other DBs (i.e. GD 61, SDSS J1242+5226, and WD 1425+540, from Farihi et al. 2013; Raddi et al. 2015; Xu et al. 2017 respectively) with a high oxygen content interpreted as accretion of water-bearing debris. Those three DBs also have a high hydrogen abundance. Hydrogen could either be primordial (Koester & Kepler 2015) or from accretion over multiple events throughout the WD's cooling history, as H never sinks. Recently, it has been found that there is a correlation between the presence of hydrogen and heavy elements (Gentile Fusillo et al. 2017). DBs with a large amount of hydrogen may imply accretion of water-rich planetesimals. However, WD 1232+563 does not have enough hydrogen – only 9% of the oxygen could be combined with hydrogen to form H_2O. This is

[3] FeO is a more common form of iron oxide but here we took Fe_2O_3 to be more conservative with the oxygen budget in the system.

Table 5. Optical and UV Abundance Comparison

Name	Atm	T (K)	log g	log n(C)/n(H(e))	log n(O)/n(H(e))	log n(Si)/n(H(e))	log n(Fe)/n(H(e))	Ref
PG 1015+161^{o}	H	20420	8.11	...	...	-5.42 ± 0.21	-4.92 ± 0.20	*this paper*
PG 1015+161^{uv}	H	19200	8.22	< -8.00	-5.50 ± 0.20	-6.40 ± 0.20	-5.50 ± 0.30	Gänsicke et al. (2012)
WD 1226+110^{o}	H	23500	8.16	...	...	-4.64 ± 0.15	< -4.50	*this paper*
WD 1226+110^{uv}	H	20900	8.15	- 7.50 ± 0.20	-4.55 ± 0.20	-5.20 ± 0.20	-5.20 ± 0.30	Gänsicke et al. (2012)
WD 1929+012^{o}	H	20890	7.90	< -4.15	-3.62 ± 0.05	-4.24 ± 0.07	-4.43 ± 0.09	Vennes et al. (2010)
WD 1929+012^{o}	H	23470	7.99	< -4.85	-3.68 ± 0.10	-4.35 ± 0.11	-4.10 ± 0.10	Melis et al. (2011)
WD 1929+012^{uv}	H	21200	7.91	-6.80 ± 0.30	-4.10 ± 0.30	-4.75 ± 0.20	-4.50 ± 0.30	Gänsicke et al. (2012)
PG 0843+517^{o}	H	24670	7.93	...	...	-4.59 ± 0.12	-3.84 ± 0.18	*this paper*
PG 0843+517^{uv}	H	23095	8.17	-7.30 ± 0.30	-5.00 ± 0.30	-5.20 ± 0.20	-4.60 ± 0.20	Gänsicke et al. (2012)
GD 40^{o}	He	15300	8.00	...	-5.61 ± 0.09	-6.76 ± 0.08	-6.48 ± 0.12	Klein et al. (2010)
GD 40^{uv}	He	15300	8.00	-7.80 ± 0.20	-5.68 ± 0.10	-6.28 ± 0.10	-6.46 ± 0.10	Jura et al. (2012)
G 241-6^{o}	He	15300	8.00	...	-5.60 ± 0.10	-6.78 ± 0.06	-6.76 ± 0.06	Klein et al. (2011)
G 241-6^{uv}	He	15300	8.00	< -8.50	...	-6.55 ± 0.10	-6.86 ± 0.10	Jura et al. (2012)
GD 61^{o}	He	17280	8.20	< -8.80	...	-6.85 ± 0.09	< -7.50	Farihi et al. (2011)
GD 61^{uv}	He	17280	8.20	< -9.10	-6.00 ± 0.15	-6.82 ± 0.12	-7.6 ± 0.3	Farihi et al. (2013)
Ton 345^{o}	He	18700	8.00	-4.63 ± 0.19	-4.58 ± 0.10	-4.91 ± 0.12	-5.07 ± 0.10	Jura et al. (2015)
Ton 345^{uv}	He	19780	8.18	-4.90 ± 0.20	-4.25 ± 0.20	-4.80 ± 0.30	-4.60 ± 0.20	Wilson et al. (2015)

^{o} Abundance measurements from the optical data.

^{uv}Abundance measurements from the UV data.

the only system known so far that has accreted O-rich but H-poor material. The next most likely O carrier is C to form CO_2. Unfortunately, from optical observations, we can only derive an upper limit, log n(C)/n(He) < -4.0. The accreting material could be rich in C but still escape optical C detections.

WD 1551+171: accretion from a refractory-enhanced parent body: The mass fraction of Ca is 6.4%, about a factor of 4 higher than the value in bulk Earth. In fact, the mass fractions of all the refractory elements, including Ca, Ti, and Al, are enhanced in WD 1551+171. This object has accreted one of the most refractory rich objects in all WDs, as shown in Fig. 2. Likely, the parent body was originally formed at a distance closer to the central star to incorporate a higher fraction of refractory elements, as has been proposed for the formation of refractory-dominated planetesimals (Carter-Bond et al. 2012). However, the accreted material is still not as refractory rich as the calcium aluminum inclusions (CAIs), whose calcium mass fractions can be up to 25% (Grossman 1980). We found no evidence for refractory dominated planetesimals in our current sample, confirming results from previous studies (Jura & Xu 2013).

WD 2207+121: accretion from a "normal" parent body. Out of the three DBZs analyzed in this study, WD 2207+121 has accreted from a planetesimal that is most similar to the bulk Earth. O, Mg, Si and Fe consist of 95% of the total mass though there is a slight enhancement of oxygen. To fully assess the nature of the accreting material, the abundances of volatile elements, such as C, S and N, need to be determined. Unfortunately, these elements only have strong transitions in the UV and optical observations are not very constraining (e.g. Jura et al. 2012; Gänsicke et al. 2012). Future observations in the UV will better constrain the nature of the accreting object.

PG 1015+161 & PG 0843+517: accretion from iron-rich objects. PG 1015+161 has accreted from a parent body with 61% Fe by mass from UV studies and the fraction goes up to 88% using optical abundances. For PG 0843+517, it is 75% from the UV and 93% from the optical, as shown in Fig. 2. Even though there are

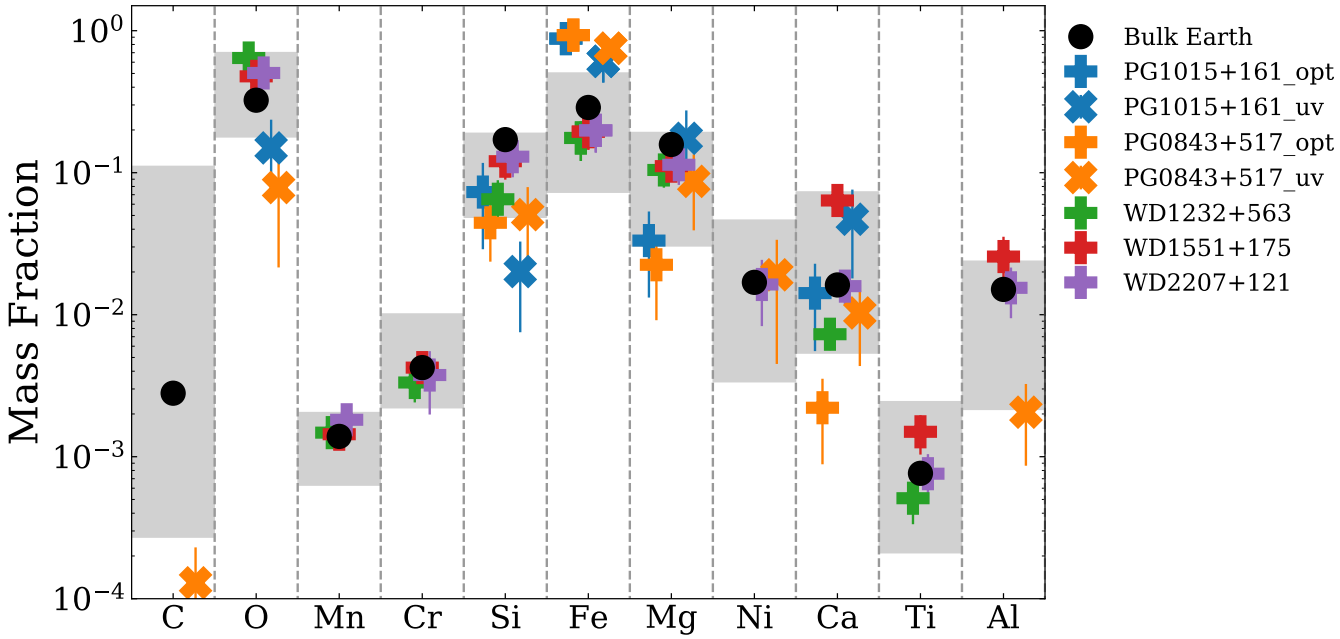

Figure 2. Mass fractions of different elements in the accreting material onto 5 WDs analyzed in this paper. Both optical and UV abundances are shown for PG 1015+161 and PG 0843+517. For clarity, only positive detections are marked. The grey shaded area indicates the range observed in all other 16 WDs with the major rock forming elements detected. The elements are arranged in the order of increasing condensation temperature.

discrepancies between the absolute abundances, the relative Fe fractions are very high and these are among the most iron-rich objects known to date. Possibly, they are a result of accretion of core-like material (Harrison et al. 2018). Previously, accretion from iron-rich objects has been identified in two other DZs, i.e. SDSS J0823+0546 and SDSS J0741+3146 (Hollands et al. 2018). A potential issue there is that neither Si nor O is detected in those two systems and it is hard to derive the nature of the material without the abundances of all the major elements.

4.2. *Dusty v.s. non-Dusty WDs*

Between 1-4% of WDs display infrared excess from dust disks, but the fraction of WDs that show pollution can be as high as 50% (Zuckerman et al. 2003, 2010; Barber et al. 2014; Koester et al. 2014; Wilson et al. 2019). Here, we compare pollution levels in WDs with and without a dust disk, as shown in Fig. 3. In addition to WDs analyzed in this study, we also include the 16 WDs with all the major elements detected (see Section 4.1) and some WD abundances from the literature (Koester et al. 2011, 2014; Koester & Kepler 2015; Hollands et al. 2018). The total mass accretion rate is calculated from the magnesium abundance, assuming that it is 15.8% of the total mass, as that in bulk Earth (Allègre et al. 2001). WDs cooler than 5000 K have no diffusion timescales calculated from the Montreal White Dwarf Database (Dufour et al. 2017) and are excluded in this figure. Previous work often extrapolates the overall accretion rate from calcium, which is the most easily detectable heavy element in the optical. However, as shown in Fig. 2, the mass fraction of calcium varies by two orders of magnitude in different WDs while the mass fraction of magnesium has a much smaller spread. In addition, magnesium is a major element in the accreting material and we consider the numbers derived from magnesium a better representation of the true accretion rate.

Before comparing properties of different systems, there are three systematics to be aware of:

Detection limits of heavy elements: it is much harder to detect heavy elements in hot WDs compared to cool ones. For example, the equivalent width of Ca II 3933 Å is 30mÅ in PG 0843+517. At the temperature of 21700 K, a calcium abundance log n(Ca)/n(H) = -6.26 is derived (see Table 2). In comparison, for WD 1344+106, a DA at 6945 K with a similar strength of Ca II 3933, the calcium abundance is -11.13 (Zuckerman et al. 2003).

Detection limits of dust disks: It is still an open question why some polluted WDs have a disk while others do not. It could be that there are small disks that escaped infrared detection or the accretion is supplied by a pure gas disk that does not produce any spectroscopic sig-

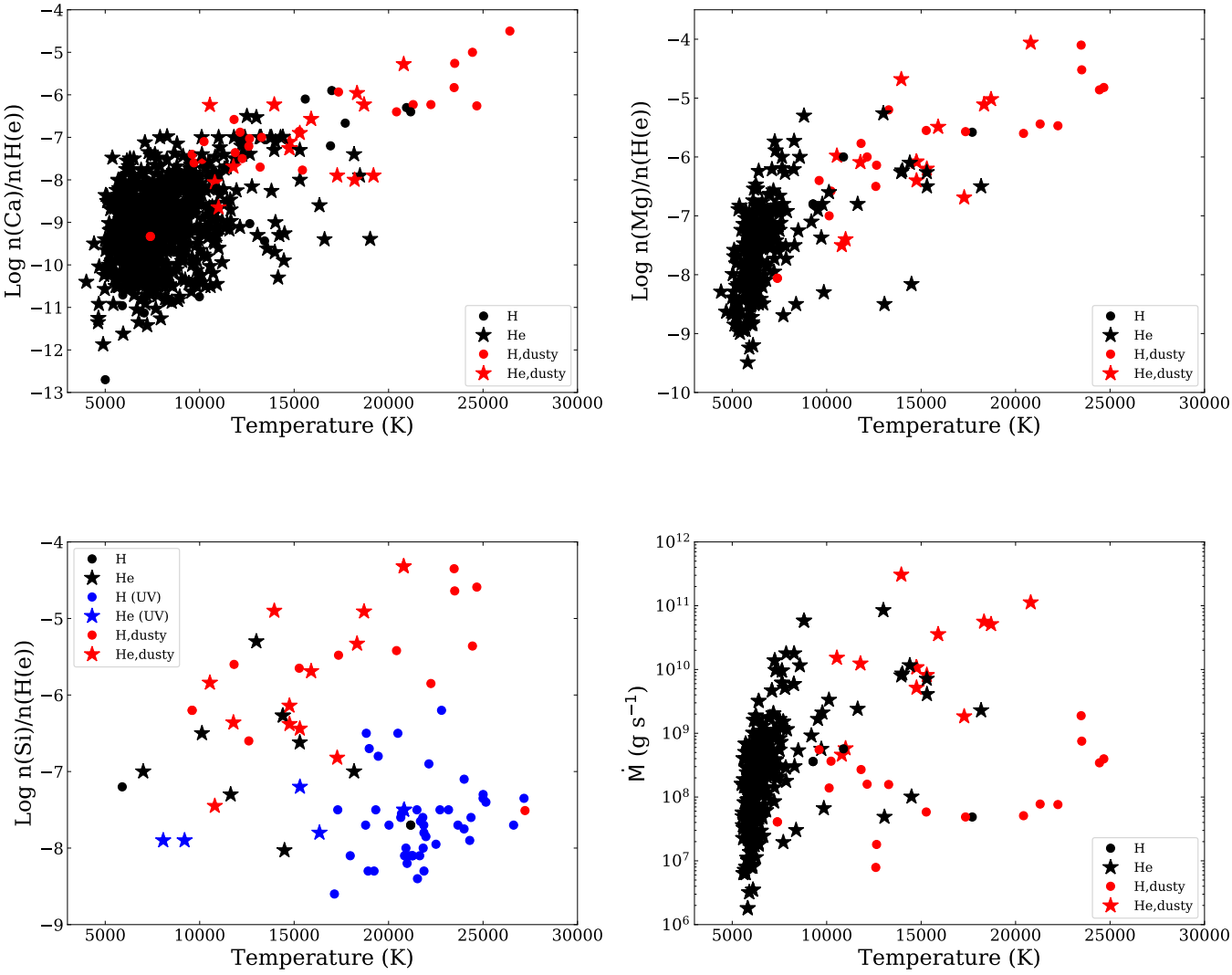

Figure 3. Ca, Mg, Si abundances, and the overall accretion rates in polluted WDs as a function of WD temperature. All the abundances are from optical observations, except for the blue points, which are from the UV.

Table 6. Pollution Level Comparison

	H	H, dusty	He	He, dusty
Log n(Ca)/n(H(e))	-7.11 ± 1.40	-5.64 ± 1.25	-8.28 ± 1.44	-6.24 ± 0.96
Log n(Mg)/n(H(e))	-6.02 ± 0.54	-5.10 ± 0.95	-6.94 ± 1.49	-4.99 ± 0.98
Log n(Si)/n(H(e))	-7.24 ± 0.83[a]	-5.06 ± 0.65	-6.33 ± 1.18	-5.15 ± 0.82
Log $\dot{M}$ (g s^{-1})	8.68 ± 0.22	8.48 ± 0.63	9.13 ± 1.99	10.68 ± 0.74

[a]This is mostly from UV measurements in Koester et al. (2014).

Note—These are average values for the WDs presented in Fig. 3.

natures; alternatively, the dust disk can be completely accreted but the heavy elements have not fully settled (Jura 2008; Bonsor et al. 2017). As shown in Fig. 3, most dust disks are detected around hot WDs and there are very few around WDs cooler than 10,000 K (Xu & Jura 2012). As a result, the dusty and non-dusty WDs shown in Fig. 3 span different temperature ranges.

Optical & UV discrepancy. Most of the abundances are from optical observations, except for Si in hot DAs (blue dots in Fig. 3). These are from *HST* UV observations reported in Koester et al. (2014). Admittedly, UV spectroscopy is more sensitive to small amounts of pollution. But it is still surprising that none of the DAs in the UV sample have as high of a Si abundance as those DAs observed in the optical. This presents an additional support of a systematic optical and UV discrepancy discussed in Section 3.3

With these three caveats in mind, here is a summary of the findings based on Fig. 3 and Table 6.

The accretion rates in He-dominated WDs are higher than those in H-dominated WDs. The largest difference is between dusty DAZs and DBZs, whose average accretion rates differ by a factor of 100. DBs have much longer settling times ($\sim 10^5$ yr) and the accretion rate represents an average historical rate. While in DAs, the settling times are ~ 1 to 10^3 yr and the accretion rate is essentially instantaneous. As a result, DAs probe continuous events while DBs probe long-term activity (Farihi et al. 2012). The difference in the accretion rate can be used to constrain the accretion history: small planetesimals are accreted continuously while accretion of larger bodies are stochastic events (Wyatt et al. 2014). Alternatively, the difference in the accretion rates could be related to inaccurate WD modeling, e.g. convective overshooting, thermohaline effect, etc (e.g. Bauer & Bildsten 2019; Cunningham et al. 2019).

There is an overall trend of decreasing pollution level as a WD cools. But this trend disappears after correcting for element settling and the change of the convection zone size. The absolute Ca and Mg abundances decrease as the WD cools and this can be explained as a result of a decreasing amount of unstable minor planets around cooler WDs (e.g. Chen et al. 2019). However, we find no significant trend for the overall accretion rate, which is related to absolute abundances, convection zone size, and settling time, as a function of the WD temperature. A statistical analysis using the calcium abundances arrives at the same conclusion – there is no age dependence of the accretion rate (Wyatt et al. 2014). This constant accretion rate poses a challenge for dynamical studies to continuously produce tidal disruption events over billions of years (e.g. Frewen & Hansen 2014).

There is no strong difference between WDs with and without a dust disk, in terms of absolute calcium, magnesium, silicon abundances, and the overall mass accretion rate. The high pollution level and dust disk connection has been recognized since von Hippel et al. (2007) and confirmed in follow up studies (e.g. Bergfors et al. 2014). However, we caution here that the spread is big and pollution is only slightly elevated in dusty WDs. In addition, there is not much overlap in the temperature range between dusty and non-dusty WDs. For non-dusty WDs, the calcium and magnesium measurements are mostly around WDs cooler than 10,000 K while dusty WDs are all between 10,000 K and 25,000 K. Due to the detection limit, only the more heavily polluted hot WDs can be identified. Future observations around hot non-dusty WDs can help filling in the gap and understanding the potential differences between dusty and non-dusty WDs.

4.3. *Mg/Ca - Si/Ca Ratios*

In the optical, Ca, Mg, and Si are the most commonly detected elements in polluted WDs. A comparison of their abundance ratios is shown in Fig. 4. The Mg/Ca ratios vary from 1 to 60 while the Si/Ca ratios vary from 1 to 45; the spread is much larger than that which is measured in CI chondrites.

No difference is found between the abundance ratios measured in DAZs and DBZs. This is not surprising because we did not expect any differences between compositions of planetary debris around DAs and DBs. However, DAZs tend to have short settling times, e.g. days to years, much shorter than 10,000 – 1000,000 yrs found for DBZs. Fig. 4 shows that settling does not play a significant role in the abundances measured in polluted WDs.

Somewhat surprisingly, Fig. 4 does not show any difference between the abundance ratios for WDs with and without a dust disk either. Previously, it has been suggested that WDs without a disk might be accreting from many smaller planetesimals while WDs with an infrared excess are accreting from one large planetesimal (Jura 2008). A mix of planetesimals could create different chemical signatures in polluted WDs but it is not observed in this sample.

The spread in the measured Mg/Ca and Si/Ca ratios could come from the intrinsic difference of the material polluting WDs. Here, we explore three additional processes that could lead to the spread.

4.3.1. *Differential Settling*

The accretion/diffusion scenario in a WD's atmosphere has been studied extensively and there are three main stages, i.e. build-up, steady-state, and decaying.

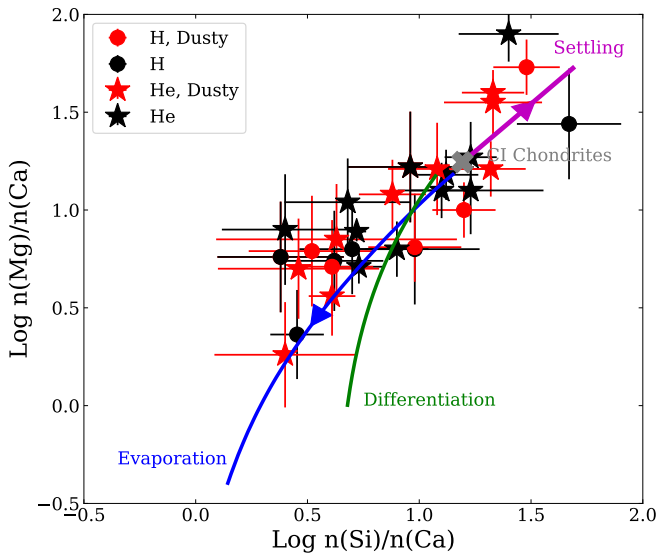

Figure 4. Mg/Ca - Si/Ca ratios in polluted WDs. There is a large spread in these ratios but there is not any clear difference between DAs and DBs, or between WDs with and without a dust disk. Starting with the composition of CI chondrites (grey cross), we computed three models, i.e. differential settling (magenta), igneous differentiation (green), and evaporation (blue). The spread of these ratios can be explained as a result of evaporation. Alternatively, the spread can be from the intrinsic difference of material that pollutes the WDs.

(Dupuis et al. 1993; Koester 2009). In the build-up stage, the measured abundance ratios in the WD's photosphere is equal to the abundance ratios in the parent body.

$$\frac{n(A)}{n(B)}_{\rm WD} = \frac{n(A)}{n(B)}_{\rm par} \quad (1)$$

In the steady-state, the measured abundance ratios are modified by the ratio of settling times, which is denoted as $\tau_{\rm A}$ and $\tau_{\rm B}$, respectively. In this case,

$$\frac{n(A)}{n(B)}_{\rm WD} = \frac{n(A)}{n(B)}_{\rm par} \times \frac{\tau_{\rm A}}{\tau_{\rm B}} \quad (2)$$

In the decaying phase, accretion has stopped and the abundances decrease exponentially. The abundance ratios are dependent on the time, t, from which the accretion has stopped. The decaying phase displays the largest variations in terms of abundance ratios.

$$\frac{n(A)}{n(B)}_{\rm WD} = \frac{n(A)}{n(B)}_{\rm par} \times \frac{e^{-t/\tau_{\rm A}}}{e^{-t/\tau_{\rm B}}} \quad (3)$$

WDs with a dust disk are often assumed to be in steady-state accretion (Equ. 2) while WDs without a disk can be in the any of the three stages (Equ. 1 - 3).

Starting with the composition of CI chondrites, we explore the effects of differential settling on abundance ratios. Even though the settling timescales are dependent on WD parameters, for polluted WDs in Fig. 4 (T>10,000 K), Ca always has the shortest settling time compared to Mg and Si. From build-up (Equ 1) to steady-state (Equ 2) to decaying phase (Equ 3), Si/Ca and Mg/Ca both become larger and the ratio moves to the top right of Fig. 4. We experimented with different sets of WD parameters and the results are similar. The settling calculation presented in Fig. 4 is for a helium-dominated atmosphere at 10,000 K. The changes of element ratios from differential settling cannot explain the observed spread. This is further supported by the fact that the scatter is observed in both DAZs and DBZs, which have orders of magnitude difference in settling times. In summary, differential settling cannot explain the large spread in Si/Ca and Mg/Ca ratios observed in polluted WDs.

4.3.2. *Igneous Differentiation*

The large spread in the Fe fractions in polluted WDs have been interpreted as a result of igneous differentiation and collision (e.g. Xu et al. 2013; Jura et al. 2013). For example, WDs accreting from fragments of a differentiated body, i.e. crust or core, would display different fractions of Fe. Here, we explore the effect of igneous differentiation on the Mg/Ca-Si/Ca ratios.

The green curve in Fig. 4 represents our calculation for igneous differentiation using the pMelts program (Ghiorso et al. 2002) with an Earth-like mantle starting composition at low pressure. The curve shows the melt composition as it evolves towards higher concentrations of Si and Ca and lower concentrations of Mg. There is a continuous removal of crystals as the melt cools from 1800 K to 1470 K. Even though igneous differentiation would change Si/Ca and Mg/Ca ratios in the same direction as the data, the curve gives a poor overall fit.

4.3.3. *Evaporation*

Another possibility is that we are witnessing an evaporation sequence of disrupted planetesimals surrounding the WDs. The chemical effects of evaporation are determined by two competing processes, i.e. the rate at which the evaporating fragment shrinks and the rate of element diffusions within the melting fragment itself. If the fragment evaporates much more rapidly than the element diffusion time, the composition of the accreting material is unaffected by evaporation. Conversely, if the rate of element diffusion is faster than the rate of evaporation, an evaporation sequence will be observed in the abundances patterns of the WD's atmosphere.

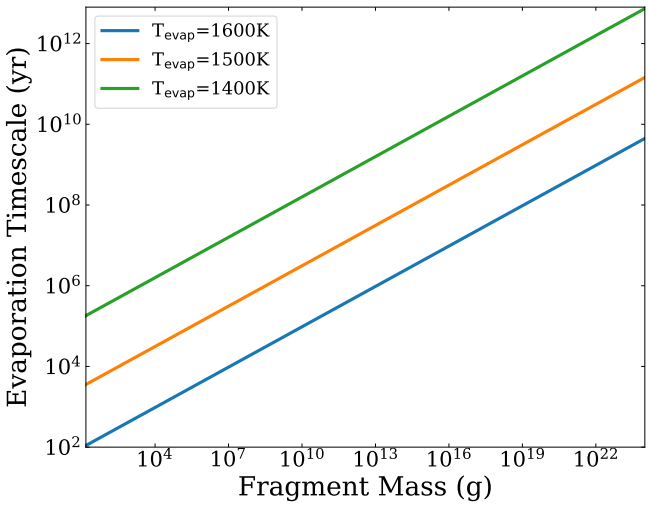

Figure 5. Evaporation timescale as a function of fragment mass. Three different evaporation temperatures were considered, T_{evap} = 1600 K, 1500 K, and 1400 K, respectively.

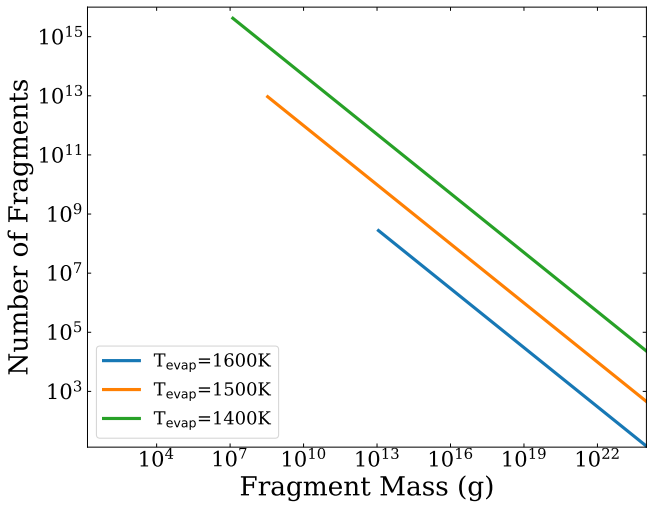

Figure 6. Number of fragments as a function of fragment mass in order to produce an accretion rate of 10^8 g s^{-1} as observed in many polluted WDs. We include three different evaporation temperatures, i.e.1600 K, 1500 K, and 1400 K.

Here, we model evaporation using the methods described by Young et al. (2019) and Young et al. (1998). In these calculations, a CI chondrite bulk composition is projected into the CaO-MgO-Al_2O_3-SiO_2 (CMAS) system where the evaporation rates are well calibrated experimentally (Richter et al. 2002). We calculated a representative curve of chemical fractionation from evaporation for a 10^{13}g (100m radius) object evaporating at 1500 K, as shown in Fig. 4.

Based on the similarity of the trajectory of evaporation and the polluted WD data in Fig. 4, we speculate that chemical fractionation by evaporation might be an explanation for the spread in Mg/Ca and Si/Ca ratios. Under this scenario, the evaporation timescale must be much longer than both the accretion time and the settling time. The accretion timescales are quite uncertain. One limit is the Poynting-Roberson drag timescale, which is several hundred years for 100 μm grains around WDs (Rafikov 2011; Bonsor et al. 2017). The longest element settling time is $\sim 10^6$ yr for cool DBZs in this sample. Fig. 5 explores evaporation timescale as a function of fragment mass. For an evaporation timescale longer than 10^6 yr, a minimum fragment mass of 10^8 g is required for an evaporation temperature of 1500 K.

An overall mass accretion rate of 10^8 g s^{-1} has been observed around many polluted WDs (see Fig. 3). To reproduce this accretion rate, we calculated the number of fragments as a function of the fragment mass in Fig. 6. The lower limit to the fragment mass is determined by the evaporation timescale, which needs to be larger than 10^6 yr; the upper limit is bound by the accretion rate of 10^8 g s^{-1}. Likely, the parent body was broken up into many pieces due to tidal forces and we are witnessing several fragments evaporating at the same time. This process has been observed around WD 1145+017, where transits from at least six stable periods were identified within a small semi-major axis (Vanderburg et al. 2015). These transits are probably all produced from fragments coming from one big parent body.

5. CONCLUSIONS

In this paper, we report results from spectroscopic studies of 19 WDs with infrared excesses from a dust disk or disk candidates. A majority of the data were taken with Keck/HIRES and Keck/ESI. Two systems (WD 1226+110 and WD 1346+031) in our sample were perviously reported to display calcium infrared triplet emission lines from circumstellar gas. Our observation shows that the gas emission around WD 1346+031 is likely not real.

The main results are summarized as follows.

• To zeroth order, the chemical compositions of extrasolar planetary material resembles that of bulk Earth, as shown in Fig. 2. However, we are starting to have a large enough sample to probe different compositions. WD 1232+563 is accreting from O-rich but H-poor material; WD 1551+171 is accreting from a refractory-rich object while PG 1015+161 and PG 0843+517 are accreting from Fe-rich objects.

• There is no strong difference in the pollution level between WDs with and without a dust disk (see Fig. 3). However, we caution that there are at least three caveats

in the analysis, i.e. detection limits of heavy elements, detection limits of dust disks, and optical and UV discrepancies. A uniform sample of polluted WDs is needed to understand the overall pattern between dusty and non-dusty WDs.

• There is a spread in the Mg/Ca and Si/Ca ratios in polluted WDs that cannot be explained by differential settling or igneous differentiation. Chemical fractionation from evaporation fits the data the best, as illustrated in Fig. 4. In this scenario, we can constrain the mass and number of evaporating bodies. Alternatively, it could come from intrinsic variations of the compositions of extrasolar planetary debris.

An outstanding issue in this work is the discrepancy of elemental abundances derived from the optical and UV observations; fortunately, element abundance ratios are not as heavily impacted. Self-consistent WD modeling is required to understanding the origin and push the polluted WD studies to a higher precision to study different planet formation and evolution processes.

Acknowledgements. We thank A. Bedard and P. Bergeron on useful discussions about deriving WD parameters, E. Dennihy on discussing the *SDSS* data of WD 1341+036, D. Koester on modeling PG 0010+280, and A. Bonsor, J. Harrison for useful comments on the compositions of the accreting material. Majority of the data presented herein were obtained at the W. M. Keck Observatory, which is operated as a scientific partnership among the California Institute of Technology, the University of California and the National Aeronautics and Space Administration. The Observatory was made possible by the generous financial support of the W. M. Keck Foundation. The authors wish to recognize and acknowledge the very significant cultural role and reverence that the summit of Maunakea has always had within the indigenous Hawaiian community. We are most fortunate to have the opportunity to conduct observations from this mountain.This work also uses results from the *Sloan Digital Sky Survey* (*SDSS*) and the European Space Agency (ESA) space mission *Gaia*.

This work is supported by the Gemini Observatory, which is operated by the Association of Universities for Research in Astronomy, Inc., on behalf of the international Gemini partnership of Argentina, Brazil, Canada, Chile, the Republic of Korea, and the United States of America. Additional support for this work was provided by NASA through grant number #14117 from the Space Telescope Science Institute, which is operated by AURA, Inc., under NASA contract NAS 5-26555. This work is also based on observations collected at the European Organisation for Astronomical Research in the Southern Hemisphere under ESO programme 096.C-0132.

Software: IRAF (Tody 1986, 1993), MAKEE, Matplotlib (Hunter 2007)

APPENDIX

A. OBSERVING LOG & FIGURES

The observing log is listed in Table A and some representative model fits to the data are shown in Figs. 7 to 13.

Table 7. Observing Logs

Name	V (mag)	Instrument	Resolution	Date (UT)	Time (sec)	SNR
G 166-58	15.6	HIRESb	40,000	2006 Jun 17	9600	80
		HIRESr	40,000	2012 Dec 31	1800	30
WD 2221-165	16.0	HIRESb	40,000	2012 Oct 29	2700	30
		HIRESr	40,000	2012 Aug 02	3250	25
WD 0307+077	16.0	HIRESr	40,000	2012 Dec 31	3600	20
PG 1541+651	15.5	HIRESb	40,000	2012 Apr 14	3000	25
		HIRESr	40,000	2012 Aug 02	3600	40
WD 1145+288	17.7	HIRESb	40,000	2018 Jan 01	3000	10
WD 1150-153	16.0	HIRESb	40,000	2008 Feb 13	3600	35
		HIRESr	40,000	2012 Dec 31	3600	25
GD 56	15.5	HIRESb	40,000	2007 Nov 20	2700	30
		HIRESr	40,000	2008 Nov 14, 2019 Sept 7	3900	50
WD 0107-192	16.2	UVES	22,000	2015 Dec 26	3600	20
HE 0106-3253	15.4	HIRESb	40,000	2008 Aug 07	3000	50
		HIRESr	40,000	2006 Sept 02	4800	60
PG 1015+161	15.6	HIRESb	40,000	2007 May 6, 2008 Feb 13	5400	65
		HIRESr	40,000	2008 Feb 26	3300	50
PG 1457-086	15.8	HIRESb	40,000	2012 Apr 14	3600	35
		HIRESr	40,000	2012 Aug 02	3600	35
WD 1226+110	16.4	HIRESb	40,000	2007 May 05	3000	35
		HIRESr	40,000	2008 Nov 14,15,16	5300	10
PG 1018+411	16.4	ESI	14,000	2017 Mar 07	3000	50
PG 0843+517	16.1	HIRESb	40,000	2012 Jan 15	1800	20
		HIRESr	40,000	2012 Dec 31	3600	25
WD 1341+036	17.0	ESI	14,000	2017 Apr 17	2600	50
WD 0010+280	15.7	COS	18,000	2016 Jun 10	1761	15
WD 1232+563	18.2	HIRESb	40,000	2015 Apr 11, 2016 Apr 01	10800	20
		ESI	14,000	2015 Apr 25, 2017 Mar 06	8460	65
WD 1551+175	17.5	HIRESb	40,000	2013 May 08	4800	30
		HIRESr	40,000	2015 Apr 09	6000	25
WD 2207+121	17.3	HIRESb	40,000	2012 Oct 28,29	8600	45
		HIRESr	40,000	2013 Sept 17	9600	25

Note—SNR is measured around 3940 Å for HIRESb and UVES, 6600 Å for HIRESr and ESI, and 1350 Å for COS.

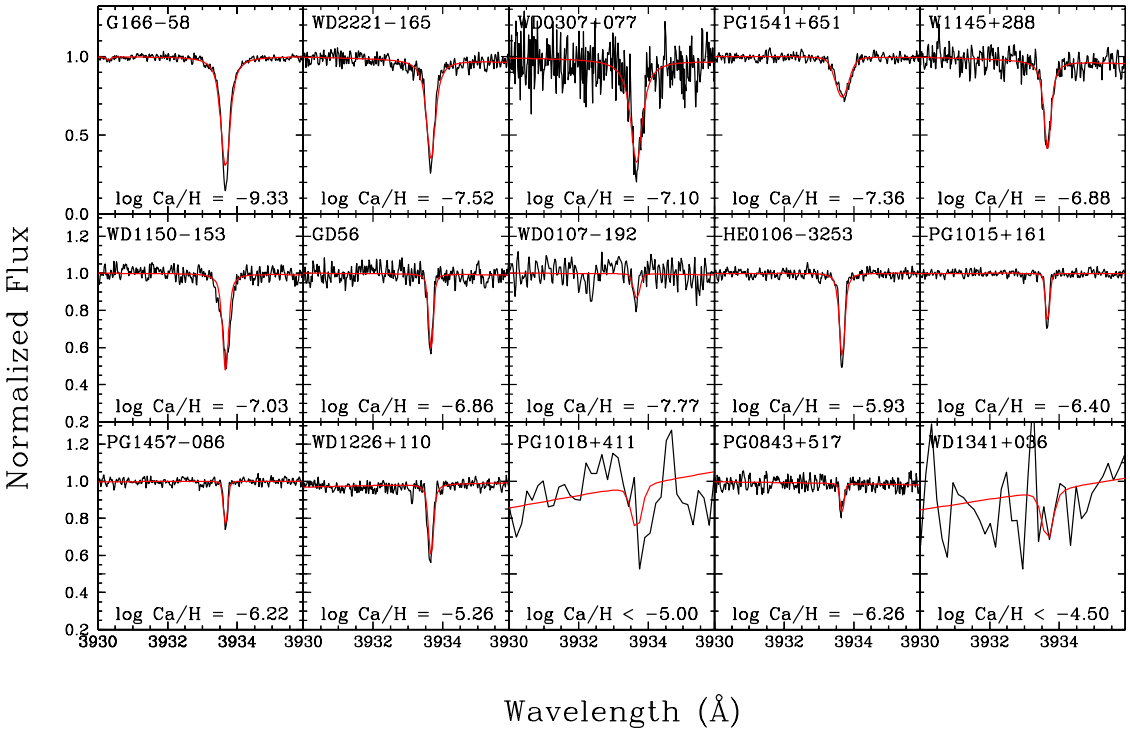

Figure 7. Calcium K 3933 Å line region for DAZs. The black and red lines represent the data and our best fit model, respectively. From top left to bottom right, the WDs are arranged in increasing effective temperature.

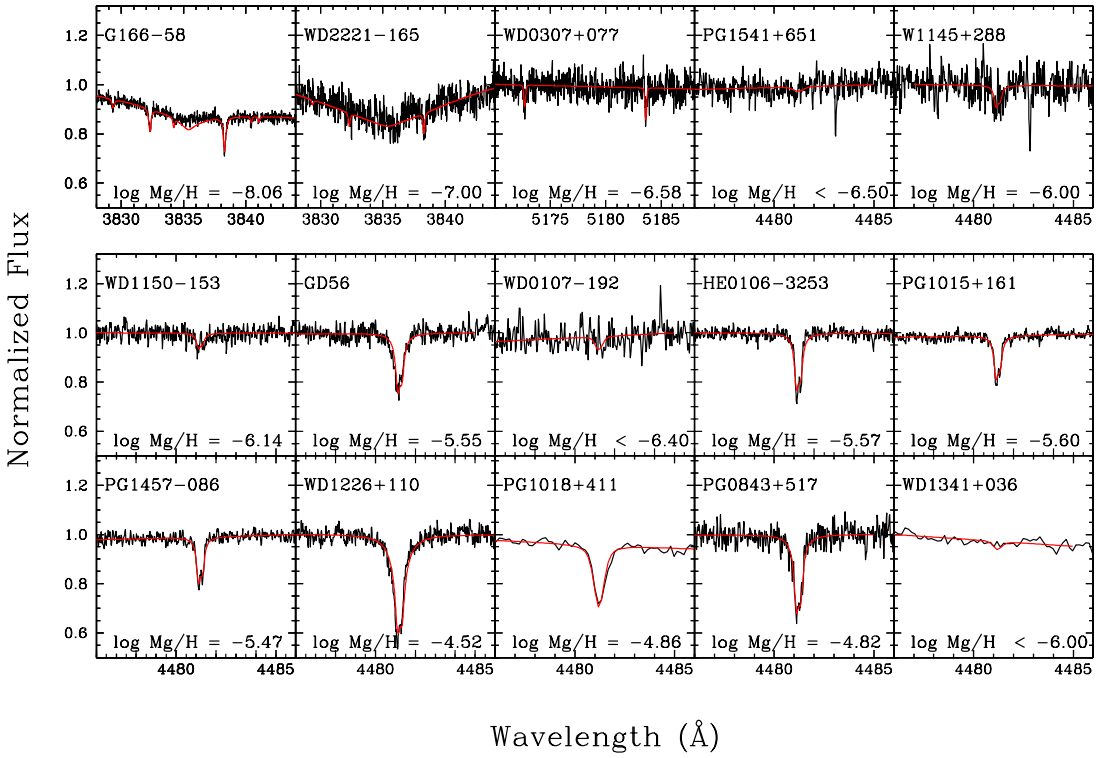

Figure 8. Same as Fig. 7 except around Mg region.

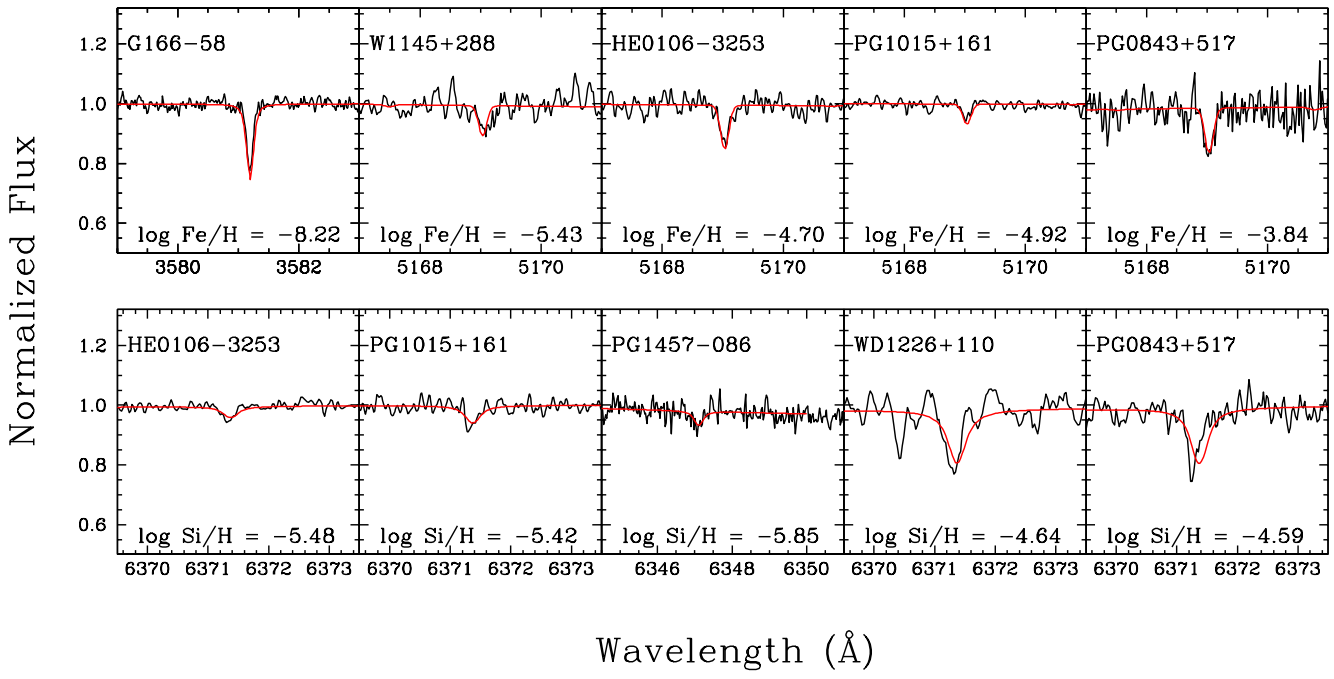

Figure 9. Same as Fig. 7 except around Fe and Si region.

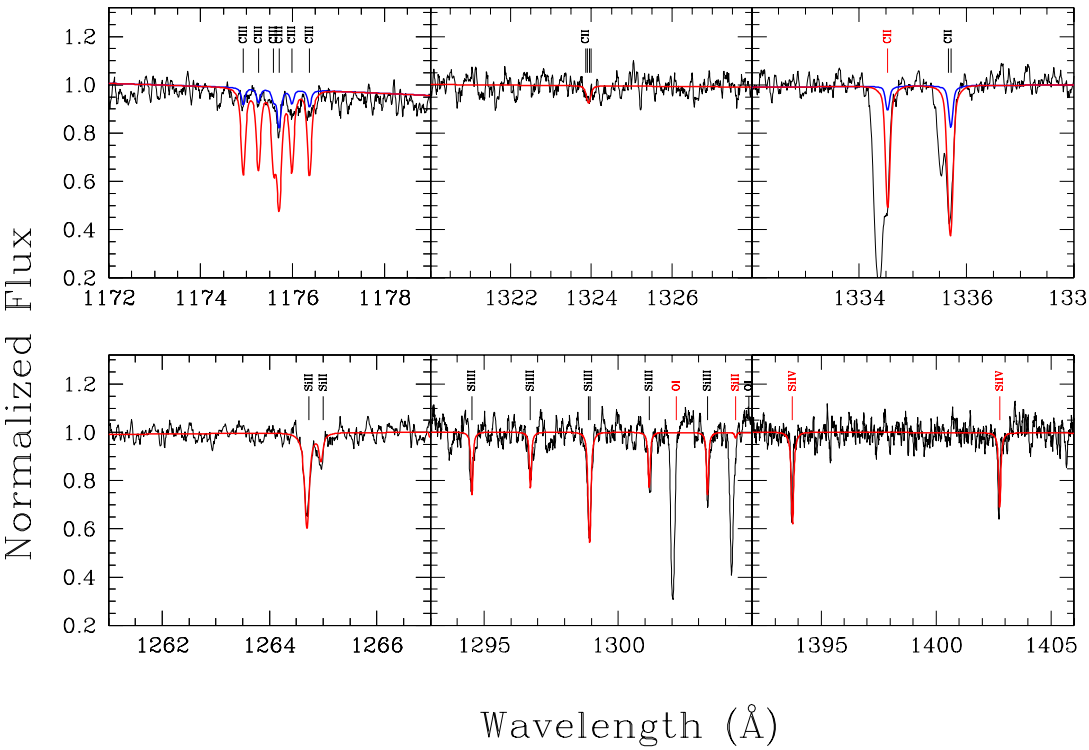

Figure 10. *HST*/COS data for PG0010+280. For carbon, two sets of models are shown, one with log n(C)/n(H) = -8.01 (blue line) that fits the C III lines; another one with log n(C)/n(H) = -6.75 (red line) that fits C II better. Red labels represent transitions from the ground state; they also show absorption from the interstellar medium in features that are blue-shifted relative to the photospheric component.

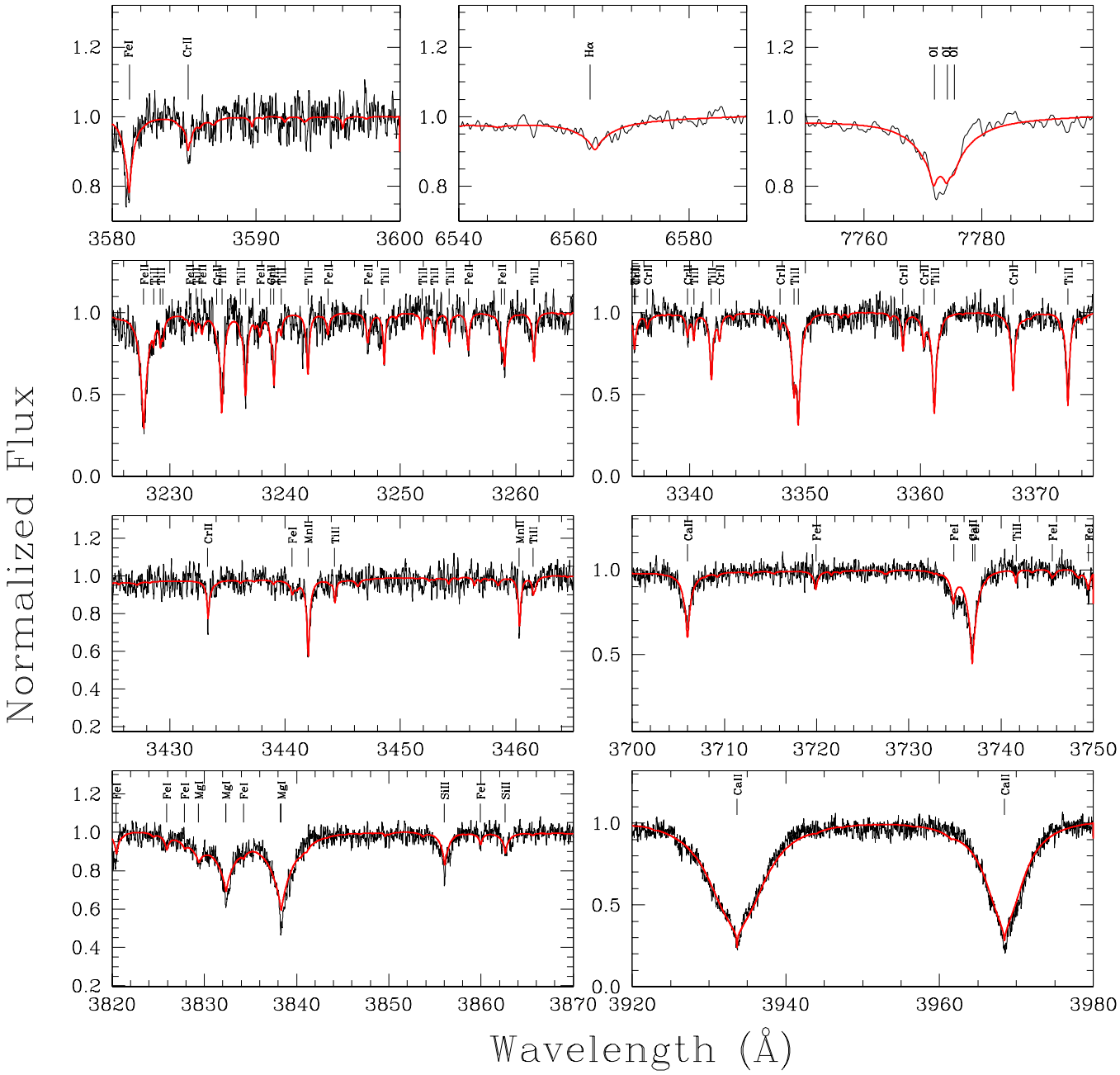

Figure 11. Best fit model on the spectra of WD 1232+563.

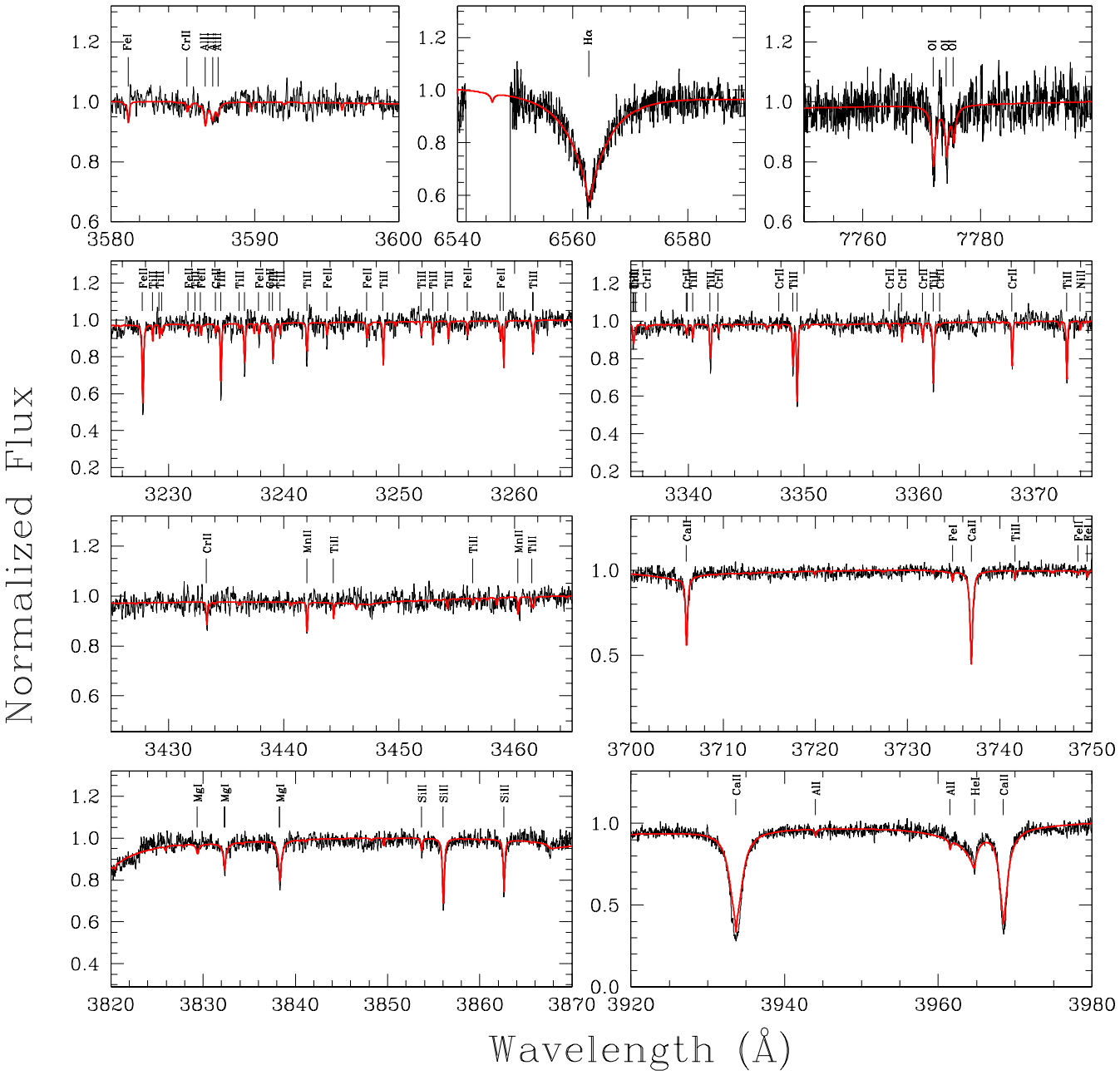

Figure 12. Best fit model on the spectra of WD 1551+175.

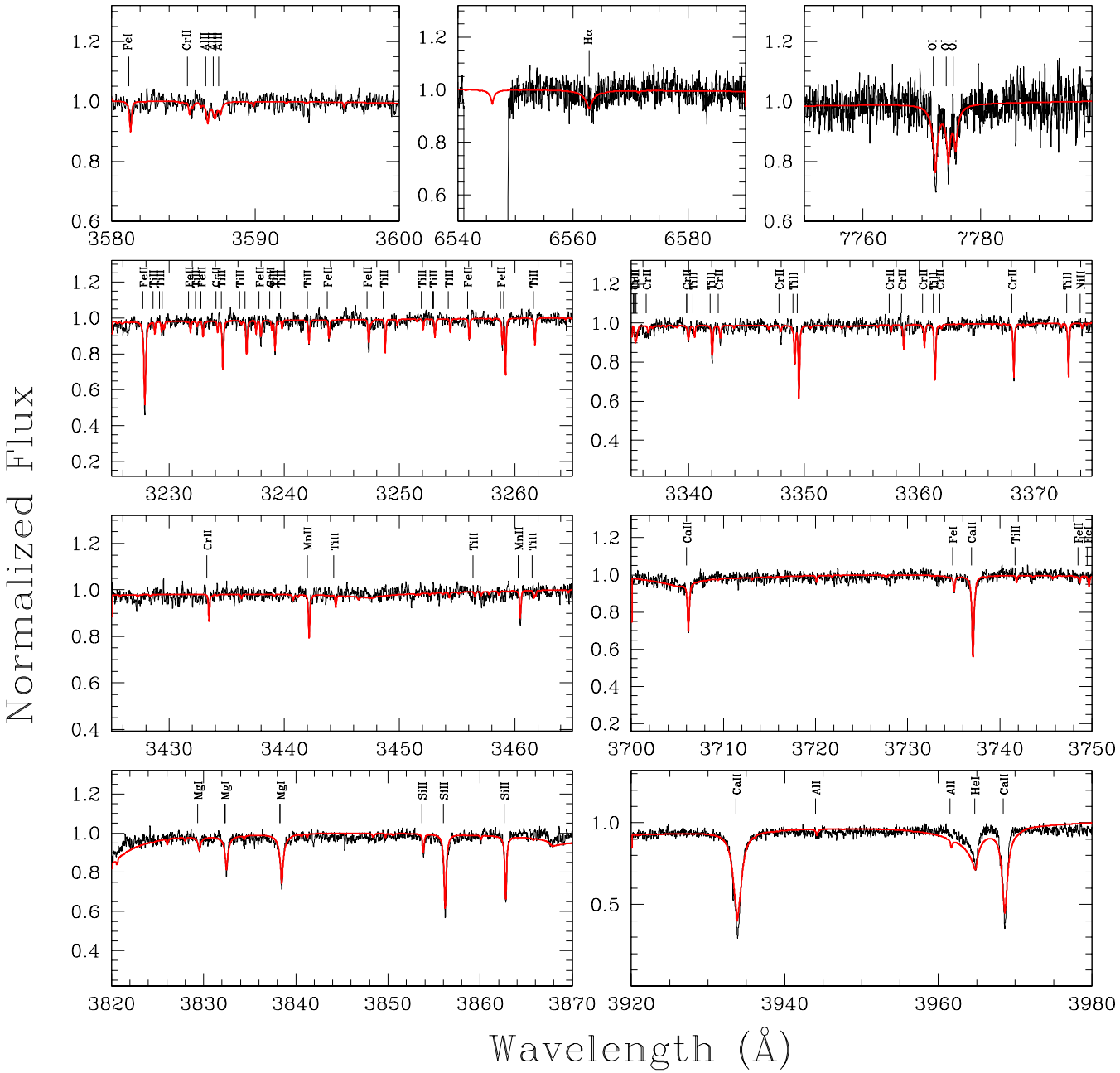

Figure 13. Best fit model on the spectra of WD 2207+127.

REFERENCES

Allègre, C., Manhès, G., & Lewin, E. 2001, Earth and Planetary Science Letters, 185, 49

Barber, S. D., Belardi, C., Kilic, M., & Gianninas, A. 2016, MNRAS, 459, 1415

Barber, S. D., Kilic, M., Brown, W. R., & Gianninas, A. 2014, ApJ, 786, 77

Bauer, E. B., & Bildsten, L. 2019, ApJ, 872, 96

Bergfors, C., Farihi, J., Dufour, P., & Rocchetto, M. 2014, MNRAS, 444, 2147

Bonsor, A., Farihi, J., Wyatt, M. C., & van Lieshout, R. 2017, MNRAS, 468, 154

Brinkworth, C. S., Gänsicke, B. T., Girven, J. M., et al. 2012, ApJ, 750, 86

Brinkworth, C. S., Gänsicke, B. T., Marsh, T. R., Hoard, D. W., & Tappert, C. 2009, ApJ, 696, 1402

Carter-Bond, J. C., O'Brien, D. P., & Raymond, S. N. 2012, ApJ, 760, 44

Chen, D.-C., Zhou, J.-L., Xie, J.-W., et al. 2019, Nature Astronomy, 3, 69

Coutu, S., Dufour, P., & Bergeron, P. et al., s. 2019

Cunningham, T., Tremblay, P.-E., Freytag, B., Ludwig, H.-G., & Koester, D. 2019, MNRAS, 488, 2503

Debes, J. H., Kilic, M., Faedi, F., et al. 2012, ApJ, 754, 59

Debes, J. H., & Sigurdsson, S. 2002, ApJ, 572, 556

Dekker, H., D'Odorico, S., Kaufer, A., Delabre, B., & Kotzlowski, H. 2000, in Proc. SPIE, Vol. 4008, Optical and IR Telescope Instrumentation and Detectors, ed. M. Iye & A. F. Moorwood, 534–545

Dennihy, E., Clemens, J. C., Debes, J. H., et al. 2017, ApJ, 849, 77

Dennihy, E., Clemens, J. C., Dunlap, B. H., et al. 2018, ApJ, 854, 40

Dorn, C., Khan, A., & Heng, K., et al. 2015, A&A, 577, A83

Dufour, P., Blouin, S., Coutu, S., et al. 2017, in Astronomical Society of the Pacific Conference Series, Vol. 509, 20th European White Dwarf Workshop, ed. P.-E. Tremblay, B. Gaensicke, & T. Marsh, 3

Dufour, P., Kilic, M., & Fontaine, G., et al. 2012, ApJ, 749, 6

Dufour, P., Bergeron, P., Liebert, J., et al. 2007, ApJ, 663, 1291

Dupuis, J., Fontaine, G., Pelletier, C., & Wesemael, F. 1993, ApJS, 84, 73

Farihi, J. 2016, NewAR, 71, 9

Farihi, J., Brinkworth, C. S., Gänsicke, B. T., et al. 2011, ApJL, 728, L8

Farihi, J., Gänsicke, B. T., & Koester, D. 2013, Science, 342, 218

Farihi, J., Gänsicke, B. T., Wyatt, M. C., et al. 2012, MNRAS, 424, 464

Farihi, J., Jura, M., Lee, J., & Zuckerman, B. 2010, ApJ, 714, 1386

Farihi, J., Jura, M., & Zuckerman, B. 2009, ApJ, 694, 805

Farihi, J., Zuckerman, B., & Becklin, E. E. 2008, ApJ, 674, 431

Frewen, S. F. N., & Hansen, B. M. S. 2014, MNRAS, 439, 2442

Gänsicke, B. T., Koester, D., Farihi, J., et al. 2012, MNRAS, 424, 333

Gänsicke, B. T., Marsh, T. R., Southworth, J., & Rebassa-Mansergas, A. 2006, Science, 314, 1908

Gentile Fusillo, N. P., Gänsicke, B. T., Farihi, J., et al. 2017, MNRAS, 468, 971

Ghiorso, M. S., Hirschmann, M. M., Reiners, P. W., & Kress, V. C. 2002, Geochemistry, Geophysics, Geosystems, 3, 1030

Gianninas, A., Bergeron, P., & Ruiz, M. T. 2011, ApJ, 743, 138

Grossman, L. 1980, Annual Review of Earth and Planetary Sciences, 8, 559

Harrison, J. H. D., Bonsor, A., & Madhusudhan, N. 2018, MNRAS, 479, 3814

Hollands, M. A., Gänsicke, B. T., & Koester, D. 2018, MNRAS, 477, 93

Hunter, J. D. 2007, Computing in Science Engineering, 9, 90

Jura, M. 2008, AJ, 135, 1785

Jura, M., Dufour, P., Xu, S., et al. 2015, ApJ, 799, 109

Jura, M., Farihi, J., & Zuckerman, B. 2007, ApJ, 663, 1285

Jura, M., & Xu, S. 2012, AJ, 143, 6

—. 2013, AJ, 145, 30

Jura, M., Xu, S., Klein, B., Koester, D., & Zuckerman, B. 2012, ApJ, 750, 69

Jura, M., Xu, S., & Young, E. D. 2013, ApJL, 775, L41

Jura, M., & Young, E. D. 2014, Annual Review of Earth and Planetary Sciences, 42, 45

Kilic, M., Patterson, A. J., Barber, S., Leggett, S. K., & Dufour, P. 2012, MNRAS, 419, L59

Kilic, M., & Redfield, S. 2007, ApJ, 660, 641

Klein, B., Jura, M., Koester, D., & Zuckerman, B. 2011, ApJ, 741, 64

Klein, B., Jura, M., Koester, D., Zuckerman, B., & Melis, C. 2010, ApJ, 709, 950

Koester, D. 2009, A&A, 498, 517

Koester, D., Gänsicke, B. T., & Farihi, J. 2014, A&A, 566, A34

Koester, D., Girven, J., Gänsicke, B. T., & Dufour, P. 2011, A&A, 530, A114+
Koester, D., & Kepler, S. O. 2015, A&A, 583, A86
Koester, D., Rollenhagen, K., Napiwotzki, R., et al. 2005, A&A, 432, 1025
Li, L., Zhang, F., Kong, X., Han, Q., & Li, J. 2017, ApJ, 836, 71
Manser, C. J., Gänsicke, B. T., Marsh, T. R., et al. 2016, MNRAS, 455, 4467
Manser, C. J., Gänsicke, B. T., Eggl, S., et al. 2019, Science, 364, 66
Melis, C., & Dufour, P. 2017, ApJ, 834, 1
Melis, C., Farihi, J., Dufour, P., et al. 2011, ApJ, 732, 90
Melis, C., Jura, M., Albert, L., Klein, B., & Zuckerman, B. 2010, ApJ, 722, 1078
Mustill, A. J., & Villaver, E. 2012, ApJ, 761, 121
Nordhaus, J., & Spiegel, D. S. 2013, MNRAS, 432, 500
Petigura, E. A., Howard, A. W., & Marcy, G. W. 2013, Proceedings of the National Academy of Science, 110, 19273
Raddi, R., Gänsicke, B. T., Koester, D., et al. 2015, MNRAS, 450, 2083
Rafikov, R. R. 2011, ApJL, 732, L3+
Richter, F. M., Davis, A. M. Ebel, D. S., & Hashimoto, A. 2002, Geochimica et Cosmochimica Acta, 66, 521
Sheinis, A. I., Bolte, M., Epps, H. W., & et al. 2002, PASP, 114, 851
Stephan, A. P., Naoz, S., & Zuckerman, B. 2017, ApJ, 844, L16
Swan, A., Farihi, J., Koester, D., et al. 2019, arXiv e-prints, arXiv:1908.08047
Tody, D. 1986, in Society of Photo-Optical Instrumentation Engineers (SPIE) Conference Series, Vol. 627, Proc. SPIE, ed. D. L. Crawford, 733
Tody, D. 1993, in Astronomical Society of the Pacific Conference Series, Vol. 52, Astronomical Data Analysis Software and Systems II, ed. R. J. Hanisch, R. J. V. Brissenden, & J. Barnes, 173
Tremblay, P.-E., Bergeron, P., & Gianninas, A. 2011, ApJ, 730, 128
Vanderburg, A., Johnson, J. A., Rappaport, S., et al. 2015, Nature, 526, 546
Vennes, S., Kawka, A., & Németh, P. 2010, MNRAS, 404, L40
Vogt, S. S., Allen, S. L., & Bigelow, B. C., et al. 1994, in Society of Photo-Optical Instrumentation Engineers (SPIE) Conference Series, ed. D. L. Crawford & E. R. Craine, Vol. 2198, 362
von Hippel, T., Kuchner, M. J., Kilic, M., Mullally, F., & Reach, W. T. 2007, ApJ, 662, 544
Wilson, D. J., Gänsicke, B. T., Farihi, J., & Koester, D. 2016, MNRAS, 459, 3282
Wilson, D. J., Gänsicke, B. T., Koester, D., et al. 2014, MNRAS, 445, 1878
—. 2015, MNRAS, 451, 3237
Wilson, T. G., Farihi, J., Gänsicke, B. T., & Swan, A. 2019, MNRAS, 1000
Wyatt, M. C., Farihi, J., Pringle, J. E., & Bonsor, A. 2014, MNRAS, 439, 3371
Xu, S., & Jura, M. 2012, ApJ, 745, 88
Xu, S., Jura, M., Dufour, P., & Zuckerman, B. 2016, ApJL, 816, L22
Xu, S., Jura, M., Klein, B., Koester, D., & Zuckerman, B. 2013, ApJ, 766, 132
Xu, S., Jura, M., Koester, D., Klein, B., & Zuckerman, B. 2014, ApJ, 783, 79
Xu, S., Jura, M., Pantoja, B., et al. 2015, ApJL, 806, L5
Xu, S., Zuckerman, B., Dufour, P., et al. 2017, ApJL, 836, L7
Young, E. D., Nagahara, H., Mysen, B. O., & Audet, D. M. 1998, Geochimica et Cosmochimica Acta, 62, 3109
Young, E. D., Shahar, A., Nimmo, F., et al. 2019, Icarus, 323, 1
Zeng, L., Sasselov, D. D., & Jacobsen, S. B. 2016, ApJ, 819, 127
Zuckerman, B., Koester, D., Melis, C., Hansen, B. M., & Jura, M. 2007, ApJ, 671, 872
Zuckerman, B., Koester, D., Reid, I. N., & Hünsch, M. 2003, ApJ, 596, 477
Zuckerman, B., Melis, C., Klein, B., Koester, D., & Jura, M. 2010, ApJ, 722, 725